

Confectionery Satellites: On the Stable Orbit of an M&M About a Human-Mass Primary

Independent Researcher*

April 2026

Abstract

We examine the conditions under which a standard plain M&M candy ($m \approx 0.91\text{ g}$, $A \approx 1.43 \times 10^{-4}\text{ m}^2$) may achieve a stable Keplerian orbit about a 70 kg human, treated as a primary. In the two-body limit, the circular orbital period at $r = 5\text{ m}$ is $\sim 12\text{ d}$ with a circulation speed of $\sim 30\text{ }\mu\text{m s}^{-1}$. However, the human’s Hill radius collapses to $\sim 34\text{ m}$ at 1 au heliocentric, and solar radiation pressure on the candy exceeds the human’s gravitational attraction for separations greater than $\sim 8\text{ cm}$. A bound but radiation-pressure-perturbed orbit at heliocentric distances $\gtrsim 200\text{ au}$ would naively be relaxed by operating in a giant-planet umbra, but this option is foreclosed by an enhanced electrostatic-charging perturbation in planetary magnetospheres; the critical floating potential at $r = 5\text{ m}$ is $\sim 3.4\text{ V}$, and equilibrium values exceed this everywhere except in the cold undisturbed local interstellar medium beyond $\sim 1000\text{ au}$ heliocentric. Additional perturbations from respiration, thermal emission, outgassing, and the non-spherical mass distribution of the primary further constrain the parameter space; a living primary is excluded outright. The Bond albedo of the candy is the only candy-specific dynamical parameter, varying the binding threshold by $\sim 20\%$ across the standard color palette. We identify two viable regimes—a frozen primary in the local interstellar medium, with the orbit bound but Coulomb-perturbed at the $\sim 25\%$ level, or operation within a drag-free spacecraft of LISA Pathfinder heritage admitting cleanly Keplerian trajectories—and discuss observational, ethical, and confectionery implications.

1 Introduction

Every massive body possesses a gravitational sphere of influence within which it may, in principle, retain bound satellites (Hill, 1878). While this fact is applied without comment to celestial bodies, its consequences for primaries of human scale appear not to have been systematically examined. The popular literature treats the inverse problem—a human standing on a small but supermassive body (Munroe, 2014)—and the formal literature on orbits about irregularly shaped primaries is well-developed in the asteroid context (Scheeres, 1994), but the specific case of a small, plausibly available test mass orbiting a human primary appears unexplored.

The problem is not entirely trivial. The human–M&M system has a mass ratio $M/m \sim 8 \times 10^4$, but absolute masses fall below those at which classical celestial mechanics is conventionally applied. Several perturbations that are negligible in standard astrodynamics—radiation pressure, thermal

*Correspondence: nfnt@synchron.city. The author thanks an anonymous large language model for assistance with the non-trivial bookkeeping of 4π factors.

emission, outgassing, electrostatic charging—become dominant. The primary is irregular in shape, generally not in mechanical equilibrium, and (in most realizations) alive.

In this paper we (i) derive the Keplerian orbital elements for the system in the two-body limit (§2); (ii) compute the human’s Hill radius across a range of operating environments (§3); (iii) quantify the dominant non-gravitational perturbations (§4); and (iv) identify the parameter regime within which stable orbits are possible (§5). We adopt a 70 kg human and a standard plain M&M ($m = 0.91$ g, equivalent disc radius $s = 6.75$ mm, density $\rho \approx 1060$ kg m^{−3}).

2 The Two-Body Problem

For a human of mass $M_h = 70$ kg approximated as a point mass, the standard gravitational parameter is

$$\mu_h \equiv GM_h \approx 4.67 \times 10^{-9} \text{ m}^3 \text{ s}^{-2}. \quad (1)$$

The circular orbital velocity and period at radius r follow as

$$v_c(r) = \sqrt{\mu_h/r}, \quad T(r) = 2\pi\sqrt{r^3/\mu_h}. \quad (2)$$

Representative values are tabulated in Table 1. A circular orbit at $r = 5$ m has $v_c \approx 31 \mu\text{m s}^{-1}$ and $T \approx 11.9$ d: speeds slower than continental drift, periods longer than a lunation. The orbital energy is correspondingly minute: at $r = 5$ m, $E_{\text{orb}} = -\mu_h m/(2r) \approx -4.3 \times 10^{-13}$ J, which is approximately the kinetic energy of a single nonpareil (~ 1 mg) rolling across a level surface at 1 mm s^{-1} .

Table 1: Circular orbital parameters for an M&M about a 70 kg human.

r [m]	v_c [$\mu\text{m s}^{-1}$]	T	Comparable timescale
0.3	125	4.2	hours
1.0	68	25.5	hours
5.0	31	11.9	days
10.0	22	33.6	days
30.0	12.5	174	days

These point-mass results establish the gravitational scale of the problem. They are, however, derived in vacuum and assume the primary to be both isolated and inert. The remainder of this paper examines the conditions under which these assumptions can be approximately satisfied.

3 Hill Sphere Analysis

The Hill radius (Hill, 1878) bounds the region within which the secondary’s gravity dominates that of an external primary M at separation a :

$$r_H = a \left(\frac{M_h}{3M} \right)^{1/3}. \quad (3)$$

For a 70 kg human in various locations, r_H takes the values shown in Table 2. At Earth’s surface and in low Earth orbit the human’s Hill radius is approximately one decimeter—less than the dimension of the primary itself, and so without practical meaning. At 1 AU heliocentric, the Hill radius reaches

Table 2: Hill radius of a 70 kg human in various gravitational environments.

Location	a	External primary M	r_H
Earth’s surface	6.37×10^6 m	$M_{\oplus} = 5.97 \times 10^{24}$ kg	0.10 m
LEO (400 km)	6.77×10^6 m	M_{\oplus}	0.11 m
Lunar surface	1.74×10^6 m	$M_{\text{moon}} = 7.34 \times 10^{22}$ kg	0.12 m
Heliocentric, 1 AU	1.50×10^{11} m	$M_{\odot} = 1.99 \times 10^{30}$ kg	34 m
Heliocentric, 30 AU	4.49×10^{12} m	M_{\odot}	1.0 km
Heliocentric, 100 AU	1.50×10^{13} m	M_{\odot}	3.4 km

34 m; in the outer heliosphere it expands to the kilometer scale, and in deep interstellar space the Hill radius is effectively unbounded.¹

The Hill radius establishes only the gravitational envelope. Within that envelope, stable orbits for an initially circular trajectory exist out to $\sim r_H/2$ for prograde orbits and $\sim r_H$ for retrograde orbits, as established numerically by Hamilton & Burns (1991); we adopt $r_H/2$ as a conservative upper bound on usable orbital radii, returning to the full operating envelope in §5.

4 Non-Gravitational Perturbations

4.1 Solar Radiation Pressure

Solar photons exert a radial outward force on the M&M of magnitude (Burns et al., 1979)

$$F_{\text{rad}}(d) = \frac{L_{\odot}}{4\pi d^2 c} A Q_{\text{pr}}, \quad (4)$$

where $L_{\odot} = 3.828 \times 10^{26}$ W, d is heliocentric distance, A is the projected cross-section of the candy, and $Q_{\text{pr}} \approx 1$ is appropriate for the opaque chocolate of a plain M&M; color-dependent variations of Q_{pr} across the standard palette are examined in §6. At 1 AU,

$$F_{\text{rad}}(1 \text{ au}) \approx 6.5 \times 10^{-10} \text{ N}, \quad (5)$$

producing an acceleration on the M&M of $a_{\text{rad}} \approx 7.1 \times 10^{-7} \text{ m s}^{-2}$. Equating this to the human’s gravitational acceleration μ_h/r^2 yields the maximum stable radius r_{max} at which the human dominates:

$$r_{\text{max}}(d) = \sqrt{\frac{\mu_h m 4\pi c}{L_{\odot} A Q_{\text{pr}}}} \cdot d. \quad (6)$$

Numerically, $r_{\text{max}}(1 \text{ au}) \approx 8.1 \text{ cm}$, which is smaller than the linear extent of the primary itself and is therefore not physically realizable. Equation (6) scales linearly in d , so naively for an orbit at $r = 5 \text{ m}$ one requires $d \gtrsim 62 \text{ au}$.²

Equation (6), however, expresses only the condition that the *radial force* balance favor the primary at the nominal orbital radius. For an actual bound trajectory two stricter conditions

¹Strictly, at separations of order one parsec the relevant external potential becomes the Galactic tide rather than the Sun, and the formal Hill construction must be replaced by a tidal-radius calculation in the local Oort frame (Heisler & Tremaine, 1986); this regime falls outside the operating envelope identified in §5 and is not pursued further.

²The treatment above neglects radiation pressure on the primary itself, $a_{\text{rad,h}} \approx 3 \times 10^{-8} \text{ m s}^{-2}$ at 1 au (5% of the M&M’s a_{rad}). Strictly, what enters the orbital equations is the differential acceleration $a_{\text{M\&M}} - a_{\text{h}}$; the threshold heliocentric distances quoted here are accordingly overestimated by a few percent, well within the precision of the analysis.

apply. Define the dimensionless perturbation $\alpha \equiv a_{\text{rad}}/(\mu_h/r_0^2)$. An energy analysis of the effective potential $V_{\text{eff}}(x, y) = -\mu_h/r - a_{\text{rad}}x$, which possesses a saddle point at $x_s = \sqrt{\mu_h/a_{\text{rad}}}$, shows that a circular initial orbit at r_0 is energetically bound only for $\alpha \lesssim 0.086$. Recognizably Keplerian (low-eccentricity) trajectories require the still more restrictive $\alpha \lesssim 0.01$. Translating to heliocentric distance for $r_0 = 5$ m: $\alpha = 1$ at $d \approx 62$ au (force balance only); $\alpha = 0.086$ at $d \approx 210$ au (binding); and $\alpha = 0.01$ at $d \approx 620$ au (cleanly elliptical).³

Figure 1 illustrates the regime numerically. At $d = 1000$ au ($\alpha = 0.004$, panel a), the orbit is a slightly precessing ellipse offset toward the anti-solar direction. At $d = 300$ au ($\alpha = 0.042$, panel b), the orbit is bound but strongly non-Keplerian: the M&M traces a teardrop-shaped trajectory and repeatedly approaches within centimeters of the primary, where multipole effects (§4.6) and the non-zero physical extent of the human invalidate the point-mass treatment entirely.

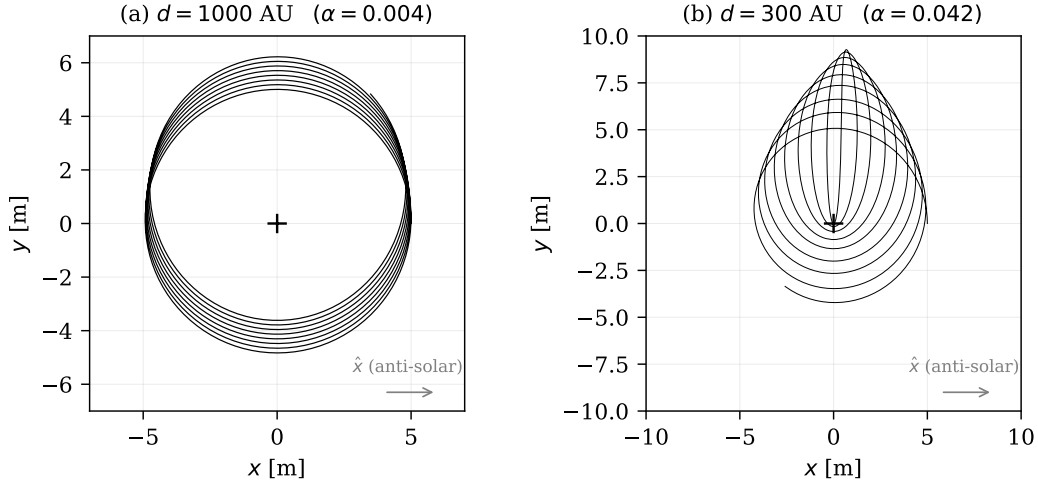


Figure 1: Numerical integration of the M&M trajectory, initial circular orbit at $r_0 = 5$ m, with constant solar-radiation force applied in $+\hat{x}$ (charging perturbations of §4.5 are not modeled here). (a) At $d = 1000$ au ($\alpha = 0.004$), the orbit is a slightly precessing ellipse, well-approximated by a Keplerian solution with small radial drift toward the anti-solar direction. (b) At $d = 300$ au ($\alpha = 0.042$), the orbit is bound but strongly perturbed; the M&M passes within 2 cm of the primary on each cycle. The cross marks the human’s center of mass. Eight orbital periods are shown in each panel. Integrator: DOP853, relative tolerance 10^{-11} .

The constraint may be relaxed by operating in optical shadow. The deepest shadows readily available in the inner Solar System are the umbrae of the giant planets; Jupiter’s umbra extends to $\sim 6 \times 10^7$ km behind the planet, providing a corridor in which radiation pressure on the M&M is suppressed by a factor of $\sim 10^6$ or more. The radiation-pressure constraint alone would therefore admit a stable orbit at 5 au heliocentric within such a shadow. This option is, however, foreclosed by the electrostatic-charging analysis of §4.5: Jovian magnetospheric plasma is hotter and denser than the local solar wind, and floating potentials in the umbra are correspondingly larger, producing a Coulomb perturbation between primary and M&M that exceeds the gravitational attraction by one to two orders of magnitude. The shadow that solves radiation pressure aggravates charging.

³This treatment assumes continuous illumination of the M&M. For an orbit at $r = 5$ m around a primary of cross-sectional radius $R_p \approx 0.2$ m, the M&M passes through the primary’s umbra for $\sim R_p/(\pi r) \approx 1\%$ of each orbit; the resulting modulation of the time-averaged radiation pressure is below the precision of the perturbation analysis and is neglected in what follows.

The same objection applies to the umbrae of the other giant planets.

4.2 The Living Primary

A living human at rest exhibits a minute ventilation of approximately 6 L min^{-1} . While the time-averaged net thrust over a full respiratory cycle approximately cancels (inhalation and exhalation reactions being nearly equal and opposite), the instantaneous mass flux of $\dot{m}_{\text{exh}} \sim 1.2 \times 10^{-4} \text{ kg s}^{-1}$ at exhalation velocity $v_{\text{exh}} \sim 1 \text{ m s}^{-1}$ produces a peak reaction thrust

$$F_{\text{exh}} \sim \dot{m}_{\text{exh}} v_{\text{exh}} \approx 1.2 \times 10^{-4} \text{ N}, \quad (7)$$

yielding peak recoil acceleration $a_{\text{exh}} \approx 1.7 \times 10^{-6} \text{ m s}^{-2}$. The relevant quantity is the resulting positional jitter of the primary's center of mass over a respiratory cycle ($\sim 4 \text{ s}$): $\Delta x \sim a_{\text{exh}} \tau^2 / 2 \sim 14 \mu\text{m}$ per breath, accumulating diffusively. This already exceeds the M&M's orbital velocity times the same interval ($v_c \tau \sim 120 \mu\text{m}$) within a small number of breaths and dwarfs the orbit radius within minutes.

The mass-ejection mechanism is essential here: by conservation of momentum, an isolated system experiences no center-of-mass drift from purely internal mass rearrangement. Cardiac activity ($\sim 70 \text{ mL}$ of blood ejected per beat, returning to the heart through venous circulation within $\sim 60 \text{ s}$), peristaltic motility ($\sim 0.01 \text{ Hz}$), and physiological tremor (limb oscillation at $8\text{--}12 \text{ Hz}$, amplitude $\sim 10 \mu\text{m}$) all involve closed mass redistribution and do not drift the COM. They modulate the primary's quadrupole moment with fractional amplitude $\Delta Q/Q \sim m_{\text{blood}} \ell_{\text{circ}}^2 / (M_h \ell^2) \sim 10^{-4}$ for cardiac activity (with comparable or smaller amplitudes for the others), at frequencies in the range $10^{-2}\text{--}10^1 \text{ Hz}$, well above the orbital frequency of $\sim 10^{-6} \text{ Hz}$. The resulting peak acceleration on the M&M at $r = 5 \text{ m}$ is $\sim (\Delta Q/Q) \mu_h / r^2 \approx 10^{-14} \text{ m s}^{-2}$, four orders of magnitude below the orbital signal, and averages to negligible effect over an orbital period. Cutaneous evaporation (perspiration, $\sim 500 \text{ g d}^{-1}$ at rest) constitutes a second mass-ejection channel of comparable magnitude to respiration.

We therefore conclude that no living human can serve as a primary, the exclusion being driven by mass-ejection mechanisms (respiration and perspiration); other commonly cited sources of biological micromotion are bounded by mass conservation. We proceed under the assumption of a deceased subject.

4.3 Thermal Emission

A body at temperature T and surface area $\Sigma \approx 1.8 \text{ m}^2$ radiates power $P = \epsilon \sigma \Sigma T^4$ with emissivity $\epsilon \approx 0.95$. At physiological temperature $T = 310 \text{ K}$, $P \approx 890 \text{ W}$. Even a modest hemispheric asymmetry of order 10^{-2} produces a net photon thrust $F_{\text{therm}} \sim \epsilon \Delta P / c \approx 3 \times 10^{-8} \text{ N}$, again far exceeding the relevant gravitational scale.⁴ Cooling the primary to $T \lesssim 100 \text{ K}$ (achievable passively in deep shadow at $\gtrsim 10 \text{ au}$) reduces P by a factor of $(310/100)^4 \approx 90$, bringing F_{therm} to a tractable level. Equilibration with the local interstellar radiation field at $T \sim 3 \text{ K}$ renders thermal recoil negligible.

4.4 Outgassing

For a water-rich primary, the cooling required by §4.3 traverses a temperature regime in which sublimation of body ice produces substantial recoil thrust. The saturation vapor pressure of ice

⁴This mechanism has historical precedent on the spaceflight side: the Pioneer 10/11 anomalous acceleration of $\sim 8 \times 10^{-10} \text{ m s}^{-2}$ —initially mysterious—was ultimately resolved as anisotropic thermal emission from the spacecraft's RTGs (Turyshev et al., 2012).

falls from ≈ 611 Pa at 273 K to ≈ 0.16 Pa at 200 K to $\sim 10^{-20}$ Pa at 50 K. The corresponding Knudsen-limited mass-loss flux, combined with modest asymmetry ($\sim 1\%$) in the direction of escape from an irregular body, yields recoil accelerations of order 10^{-3} m s^{-2} at 273 K and 10^{-5} m s^{-2} at 200 K—vastly in excess of the orbital signal. The primary must therefore be allowed to equilibrate radiatively to $T \lesssim 50$ K before the M&M is deployed; the cooling time, set by emission against the local interstellar radiation field, is of order ten days for a 70 kg body of surface area $\sim 1.8 \text{ m}^2$. Synthetic substrates with low volatile content (notably the SEBS/mineral-oil composites used in commercial ballistic-gel formulations) do not exhibit this transient and may be deployed immediately upon thermal equilibration with the surrounding hardware. The M&M itself is similarly stable in the operating environment: sucrose, chocolate, and the dye-shell constituents have vapor pressures well below the chamber background at all temperatures encountered.

4.5 Electrostatic Charging

In deep space, both primary and M&M accumulate net charge from galactic-cosmic-ray bombardment, secondary-electron emission, photoemission, and ambient-plasma collection. The equilibrium floating potential V_f is set by current balance among these processes, and varies markedly with the local plasma environment (Whipple, 1981). With body capacitance $C_h \approx 4\pi\epsilon_0 R_h \sim 6 \times 10^{-11} \text{ F}$ for the primary (using effective radius $R_h \sim 0.5 \text{ m}$) and $C_{\text{m\&m}} \approx 4\pi\epsilon_0 R_{\text{m\&m}} \sim 7 \times 10^{-13} \text{ F}$ for the M&M, the Coulomb force between two bodies floating at common potential V_f at separation $r = 5 \text{ m}$ is

$$F_{\text{Coul}}(V_f) = \frac{k_e C_h C_{\text{m\&m}} V_f^2}{r^2} \approx 1.5 \times 10^{-14} \text{ N} \cdot V_f^2 \quad (V_f \text{ in volts}). \quad (8)$$

Equating to the gravitational attraction $F_{\text{grav}} = GM_h m_{\text{m\&m}}/r^2 \approx 1.7 \times 10^{-13} \text{ N}$ yields a critical floating potential

$$V_f^{\text{crit}} = \sqrt{\frac{GM_h m_{\text{m\&m}}}{k_e C_h C_{\text{m\&m}}}} \approx 3.4 \text{ V}, \quad (9)$$

above which Coulomb repulsion exceeds the gravitational attraction and the orbit is unbound; below it, $F_{\text{Coul}}/F_{\text{grav}} \approx 0.088 V_f^2$.

The threshold is restrictive. Floating potentials in solar wind plasma (electron temperature $T_e \sim 10 \text{ eV}$ at 1 au, falling to a few eV in the outer heliosphere) reach $V_f \sim -10 \text{ V}$ to -30 V on shaded surfaces, where photoemission cannot offset plasma-electron collection; the resulting $F_{\text{Coul}}/F_{\text{grav}}$ is of order 10–100. Jovian magnetospheric plasma (within Jupiter’s umbra at 5 au) is hotter and denser, with V_f similarly negative, foreclosing the umbra-shielding option of §4. The heliopause boundary layer at ~ 120 – 160 AU exhibits anomalously hot plasma ($T_e \sim 4 \text{ eV}$ from Voyager 2 *in situ* measurements (Richardson et al., 2019)) yielding $V_f \sim -10 \text{ V}$, again well above threshold.

The exception is the undisturbed local interstellar medium beyond the heliopause boundary disturbances. There the cold partially-ionized plasma ($T_e \approx 0.6 \text{ eV}$, $n_e \approx 0.07 \text{ cm}^{-3}$ (Gurnett et al., 2013)) yields $V_f \approx -1.7 \text{ V}$, giving $F_{\text{Coul}}/F_{\text{grav}} \approx 0.25$: the orbit is bound, but Coulomb-perturbed at the 25% level—a fractional perturbation comparable to the radiation-pressure case in panel (b) of Figure 1, but driven by electrostatics rather than radiation. Operationally this requires placement well past the heliopause, of order 500 au or more beyond the boundary disturbances directly observed by Voyager, hence $\gtrsim 1000 \text{ au}$ heliocentric.

Active charge neutralization—UV-induced photoemission as demonstrated on LISA Pathfinder (Armano et al., 2016)—suppresses V_f below $\sim 0.1 \text{ V}$ and eliminates the Coulomb perturbation entirely. The heliocentric configuration admits no such mitigation and must rely on whatever

passive photoemission and plasma-bath neutralization the local environment provides; the drag-free spacecraft realization is therefore the only configuration that admits a cleanly Keplerian orbit. Stochastic charging from individual cosmic-ray strikes and dust impacts is bounded by the same plasma-bath restoring current, with relaxation time $\tau \sim C/J_{\text{plasma}}A \sim 10^{-2}\text{ s}$ in the LIC; it contributes negligible time-averaged perturbation against the $\sim 10^6\text{ s}$ orbital period (kilovolt-class charging events documented in disturbed magnetospheric plasmas, see Garrett & Whittlesey 2012, do not occur in the cold LIC).

4.6 *Mass Distribution of the Primary*

The human is, geometrically, a prolate body of length $\ell \sim 1.7\text{ m}$ and mean radius $R \sim 0.2\text{ m}$. Its non-spherical mass distribution affects the orbit in three regimes: at small r through chaotic dynamics, at intermediate r through quadrupole-induced precession, and at large r negligibly.

The leading non-Keplerian term is a quadrupole (analogous to J_2) of magnitude $\sim (\ell/2r)^2$. At $r = 5\text{ m}$ the correction is $\sim 3\%$, producing secular precession of the line of apsides at a rate of order $2\pi \cdot 0.03/T \approx 2 \times 10^{-7}\text{ rad s}^{-1}$. At $r \gtrsim 10\text{ m}$ the primary may be treated as approximately spherical to better than 1%.

For close-in trajectories the question is not perturbation magnitude but dynamical stability. Scheeres (1994) showed that for orbits about uniformly rotating triaxial ellipsoids, large regions of phase space become chaotic at radii comparable to the longest semi-axis of the primary. Subsequent work on irregular asteroid shapes (Scheeres et al., 1996) found chaotic zones extending to radii of order the longest body dimension, with stable orbits emerging only beyond a few semi-axes. Applying these results to the human primary ($a \approx \ell/2 \approx 0.85\text{ m}$), trajectories at $r \lesssim 1\text{ m}$ are expected to be chaotic with a non-trivial collision probability per orbit, while $r \gtrsim 2\text{ m}$ should support quasi-periodic motion. Empirical confirmation in this regime has come from the OSIRIS-REx encounter with (101955) Bennu, where the spacecraft documented spontaneous particle-ejection events producing transient bound and escaping trajectories governed by the same combination of irregular gravity and radiation pressure considered here, at substantially larger primary mass (Lauretta et al., 2019; Scheeres et al., 2019). Our chosen operating point at $r = 5\text{ m}$ sits comfortably outside this regime; the lower bound on r in §5 is therefore set by perturbation magnitude rather than by chaos.

A rigid body in deep space rotates as a torque-free Euler top about its principal axes; in the absence of internal energy dissipation, it exhibits bounded precession rather than relaxing to a fixed orientation (Landau & Lifshitz, 1976). For a prolate human body the principal moment-of-inertia ratio (with the convention $I_1 \leq I_2 \leq I_3$, so that I_1 is the smallest moment, about the long axis) is $I_3/I_1 \sim 25$, with a precession period set by the initial angular momentum and generically incommensurate with the orbital period. The quadrupole moment thus rotates in the orbital frame on a precession timescale, converting the secular apsidal precession discussed above into an oscillating perturbation whose time-averaged amplitude remains bounded by the $\sim 3\%$ scale of the static quadrupole at $r = 5\text{ m}$. The operating regime identified in §5 is therefore unaffected.

4.7 *Subdominant Effects*

For completeness we note several effects whose magnitudes lie well below the orbital signal across all configurations considered. Drag from the solar wind and the local interstellar medium produces an acceleration on the M&M of order 10^{-14} m s^{-2} . The Yarkovsky effect (asymmetric thermal re-emission from a rotating M&M) introduces sub-percent corrections to the radiation-pressure analysis at typical rotation rates and thermal-lag timescales. Anisotropy in the galactic-cosmic-ray flux (Compton–Getting effect) contributes a body thrust of $\sim 10^{-17}\text{ N}$. Intrinsic radiogenic

heating of a 70 kg body from ^{40}K and ^{14}C ($\sim 10^{-9}\text{ W}$) is undetectable against the thermal-emission analysis of §4.3. Biological decomposition halts below $\sim 250\text{ K}$ and is suppressed in the operating regime; the SEBS glass transition near 223 K leaves the synthetic primary structurally stable when frozen. Magnetic-field interactions between charged or weakly ferromagnetic components in the ambient field ($\sim 3\text{ }\mu\text{G}$) are below threshold, and the drag-free spacecraft realization moreover provides standard magnetic shielding. Casimir forces between primary and M&M at $r = 5\text{ m}$ are of order $\hbar c \Sigma / r^4 \sim 10^{-30}\text{ N}$, with the corresponding van der Waals contribution falling as $1/r^7$; we elect not to quantify the neutrino-momentum-transfer, gravitational-wave-background, or cosmic-microwave-background contributions individually.

5 The Operating Regime

Combining the constraints from §3 and §4, the allowed parameter space for a bound M&M orbit is bounded by:

1. **Lower bound on r :** $r \gtrsim 5\text{ m}$, set by the requirement that the primary be approximately spherical (multipole correction $\lesssim 5\%$).
2. **Upper bound on r :** $r \lesssim r_H/2$ for prograde orbits (or $\lesssim r_H$ for retrograde), set by the Hill sphere of the human in the ambient gravitational environment.
3. **Heliocentric distance:** $d \gtrsim 1000\text{ au}$, set jointly by the radiation-pressure binding threshold and the floating-potential constraint of §4.5; the cold plasma of the undisturbed local interstellar medium is required to keep the Coulomb perturbation sub-gravitational. Planetary-umbra shielding does not relax this requirement, since planetary magnetospheric plasma drives floating potentials above threshold.
4. **Primary state:** structurally rigid and at thermal equilibrium with the local radiation field ($T \lesssim 100\text{ K}$); either a deceased human or a synthetic anthropomorphic substitute of equivalent mass distribution.

A canonical configuration meeting all four conditions is a frozen human cadaver placed at $\sim 1000\text{ au}$ heliocentric distance, sited well past the heliopause boundary disturbances in the cold undisturbed local interstellar medium where the floating-potential threshold of §4.5 is satisfied. With an M&M imparted a tangential velocity of $\sim 30\text{ }\mu\text{m s}^{-1}$ at a radial separation of $r = 5\text{ m}$, the orbit is bound on timescales limited primarily by interstellar dust drag (negligible over $\sim 10^4$ orbits) but Coulomb-perturbed at the $\sim 25\%$ level—qualitatively similar to the radiation-pressure-perturbed regime depicted in panel (b) of Figure 1, with electrostatic rather than radiative driving. A cleanly Keplerian realization in this configuration is precluded by the residual Coulomb force, which the heliocentric environment provides no means to neutralize.

6 Discussion

The color of the M&M enters the orbital dynamics through the radiation-pressure efficiency $Q_{\text{pr}} \approx 1 + A$, where A is the Bond albedo of the dyed shell. For the standard M&M color palette, A ranges from ~ 0.10 for brown (the underlying chocolate color) to ~ 0.55 for yellow, with red, orange, green, and blue at intermediate values. The threshold heliocentric distance for binding at $r = 5\text{ m}$ scales as $\sqrt{Q_{\text{pr}}}$, varying from $d_{\text{bind}} \approx 221\text{ au}$ for brown to $d_{\text{bind}} \approx 262\text{ au}$ for yellow—a 19% spread across the palette (Figure 2). At $d = 250\text{ au}$, brown, blue, red, and green M&Ms are bound at $r = 5\text{ m}$; orange sits at the margin; yellow escapes. These thresholds are derived from the radiation-pressure analysis alone; once the charging constraint of §4.5 is included, the operational

binding distance is set by the floating-potential threshold and is approximately independent of color, all six requiring $d \gtrsim 1000$ au. The color physics described in this section is therefore pedagogical rather than operational.

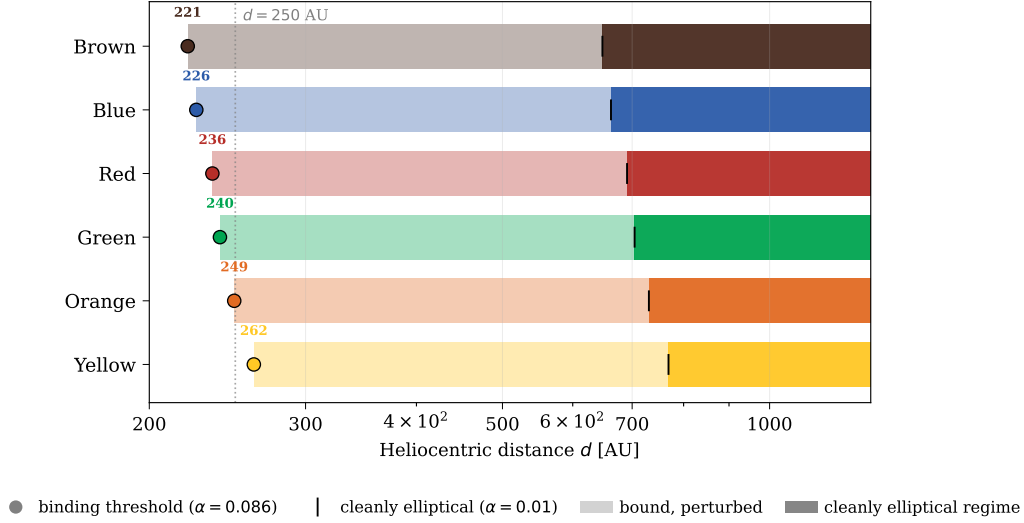


Figure 2: Stability ranges for the six standard M&M colors at orbital radius $r_0 = 5$ m. The colored circle marks the binding threshold ($\alpha = 0.086$); the black tick marks the cleanly elliptical regime ($\alpha = 0.01$). Lightly shaded regions are bound but radiation-pressure-perturbed; saturated regions are cleanly Keplerian. The vertical dotted line at $d = 250$ au marks an illustrative near-threshold distance: at this d , brown through green are bound at $r = 5$ m; orange sits at its threshold; yellow lies beyond.

The same color ordering manifests directly in the orbit geometry. Figure 3 shows one full orbital period for each color at $d = 280$ au, where all six colors are bound but radiation-pressure-perturbed. Bond albedo and orbit eccentricity track together: brown traces the tightest arc (perihelion 3.17 m, apohelion 6.58 m), and yellow the widest (2.65 m, 7.21 m), with the intermediate colors interpolating monotonically. Across the standard palette the range of perihelion distances varies by approximately 20%.

Over the course of an extended mission, this color stratification is itself transient. The FD&C dye layer photobleaches under cumulative solar UV—both the azo dyes (red, yellow) and the triarylmethane dyes (blue, green) undergo well-documented photolytic degradation, typically following pseudo-first-order kinetics in dilute conditions (Rauf & Ashraf, 2009)—driving the Bond albedo asymptotically toward the chocolate value. A bright-colored M&M deployed near its stability threshold therefore becomes increasingly bound over time, with secular drift in the threshold d_{bind} of order 20% over multi-year mission timescales. Cosmic-ray darkening of the chocolate substrate contributes a small countervailing effect. The dynamical consequence is a secular evolution unique to confectionery satellites: the orbit’s outer stability boundary slowly retreats as the M&M loses its color.

Peanut and almond variants—of mass ~ 2.3 g and ~ 2.0 g respectively—introduce no new physics, though their larger cross-section-to-mass ratio shifts r_{max} inward by approximately one third at fixed d .

Recent advances in laboratory gravity measurement provide partial analogs to the system considered here. Westphal et al. (2021) measured gravitational coupling between two 92 mg gold spheres

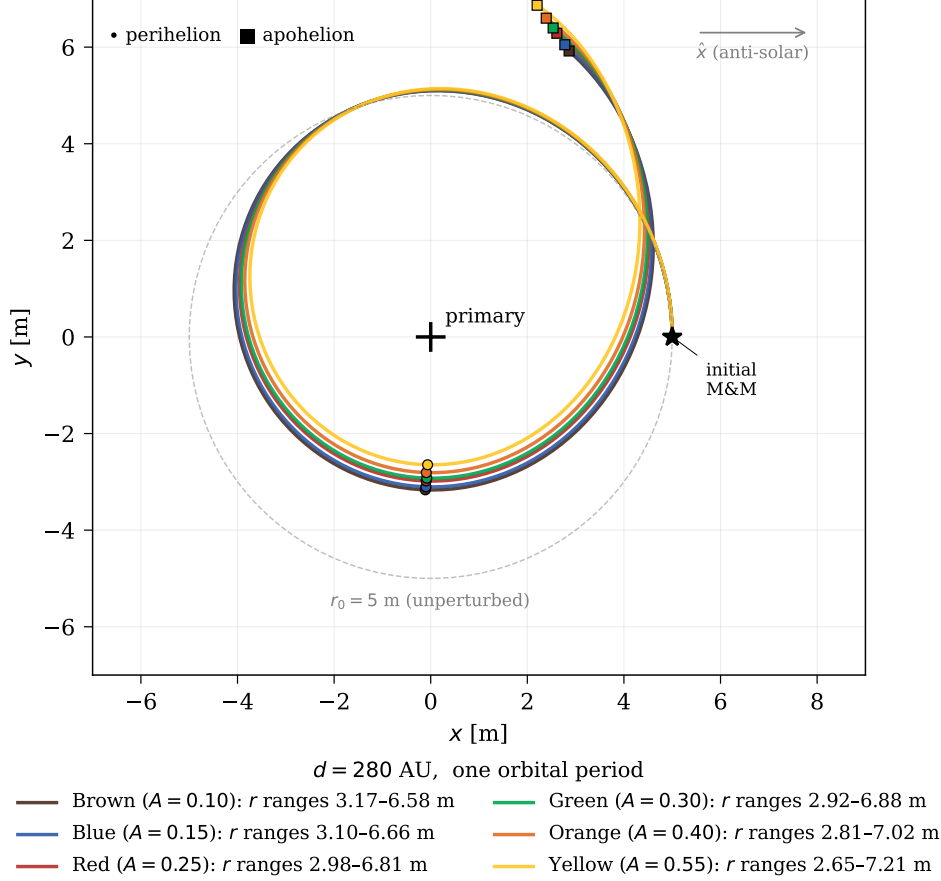


Figure 3: One orbital period for each color at $d = 280 \text{ au}$, $r_0 = 5 \text{ m}$, plotted in color order from brown (innermost) to yellow (outermost). The dashed circle shows the unperturbed circular orbit. Perihelion (closest approach to the primary) and apohelion (farthest) are marked for each color; the gradient at top and bottom reflects the monotonic dependence of orbit eccentricity on Bond albedo.

using a torsion-balance configuration; Fuchs et al. (2024) extended this to a magnetically levitated submilligram test mass in a superconducting trap. These experiments probe the gravitational *force* between small masses but cannot reproduce the orbital trajectory: Earth’s gravitational acceleration exceeds the relevant signal by approximately ten orders of magnitude, and existing free-fall facilities provide microgravity conditions for at most ~ 10 seconds against the $\sim 10^6 \text{ s}$ orbital period required. The torsion-balance constraint is fundamental rather than technical, as any laboratory configuration in which Earth’s gravity is not actively cancelled is restricted to detecting forces, not closed trajectories.

A genuine *cleanly Keplerian* orbital realization therefore requires a drag-free spacecraft. The LISA Pathfinder mission (Armano et al., 2016) demonstrated residual accelerations of order $10^{-15} \text{ m s}^{-2} / \sqrt{\text{Hz}}$ at millihertz frequencies—five orders of magnitude smaller than the M&M’s gravitational acceleration toward the primary at $r = 5 \text{ m}$. Within a sealed drag-free spacecraft, the solar radiation pressure constraint that motivates the heliocentric requirement is eliminated; the thermal-emission constraint similarly disappears, since primary, M&M, and hull may equilibrate at any common temperature without inducing differential thrust; and the electrostatic-charging perturbation that otherwise dominates even in the undisturbed LIC (§4.5) is suppressed by the

same UV-photoemission control demonstrated on Pathfinder. The spacecraft realization therefore admits cleanly Keplerian orbits in a way that no heliocentric configuration can. A successor mission stationed at L1, sized appropriately (~ 10 m enclosure for $r = 5$ m orbits)⁵ and held to ultra-high vacuum ($\lesssim 10^{-10}$ Pa to suppress residual gas drag), would in principle reproduce the orbital configuration analyzed in this paper. Cost estimates scaled to the geometric and vacuum requirements of the footnote above place such a mission in the LISA range, of order \$1–3 billion.

The choice of a deceased human as primary, while consistent with the framing of the experiment, is not strictly required by the dynamics. Any 70 kg object of approximately human geometry and density satisfies the relevant constraints. Synthetic ballistic-gel anthropomorphic dummies (Perma-Gel formulation; density $\approx 1010 \text{ kg m}^{-3}$ matched to FBI tissue-equivalent standards; full-body 95 kg variants commercially available, with custom 70 kg builds available to order)⁶ match the cadaver’s gravitational and inertial properties to within experimental tolerances, freeze rigid below 273 K with vapor pressure compatible with UHV operation, avoid the multi-day radiative cool-down required of water-rich primaries (§4.4), and circumvent the regulatory and supply-chain limitations identified in the acknowledgments. We retain the cadaver-based formulation in this work for completeness, and recommend the synthetic gel dummy for any practical implementation.

7 Conclusion

A standard plain M&M can, in principle, achieve a bound orbit about a 70 kg human. The required configuration is severely constrained: the primary must be rigid and cold (a deceased human, or a synthetic anthropomorphic substitute of equivalent mass distribution); the orbital radius must lie between approximately 5 and 30 meters; and the heliocentric configuration must reside in the undisturbed local interstellar medium beyond ~ 1000 au, where electrostatic charging is the binding constraint rather than radiation pressure. The umbra-shielding option in the inner Solar System, naively suggested by radiation-pressure considerations, is foreclosed by enhanced charging within planetary magnetospheres. Within the allowed heliocentric regime the orbit is bound but Coulomb-perturbed at the $\sim 25\%$ level; cleanly Keplerian trajectories are admitted only within a drag-free spacecraft, where active charge management and shielding eliminate both perturbations. Within these constraints, orbital periods of weeks to months and circulation speeds of tens of micrometers per second are attainable. The result generalizes straightforwardly to other small confections, with peanut and almond variants requiring proportionally more stringent conditions on heliocentric distance and brightly colored plain M&Ms requiring 20% greater heliocentric distance than dark ones, a difference that secularly relaxes as the dye layer photobleaches.

We commend this problem to the educational community as an unusually direct illustration of the relative magnitudes of gravitational and non-gravitational forces in the Solar System. We note that the cost-limiting step has, over the course of this analysis, migrated from procurement to spaceflight.

⁵The 10 m figure represents the geometric requirement only. Spacecraft self-gravity sets a separate and generally stricter scale: a Pathfinder-class hull mass (~ 125 kg) at $r = 5$ m from the M&M produces gravitational acceleration $\sim 3 \times 10^{-10} \text{ m s}^{-2}$, comparable to or exceeding the primary’s contribution. Suppression to acceptable levels requires either approximate spherical symmetry of the spacecraft mass distribution (vanishing interior field by Newton’s shell theorem) or an enclosure radius substantially larger than 10 m, since the unsuppressed contribution falls as $1/r^2$ at fixed hull mass. The realized mission is therefore likely closer to LISA than to Pathfinder in scale.

⁶Organic gelatin-based ballistic gel formulations should not be used for this application: they decompose within 2–3 weeks of casting even under refrigeration, replicating the very cadaveric instabilities that motivated the substitution.

Acknowledgments

The author confirms that no human subjects were harmed in the preparation of this manuscript. Harm to the subject is, as established in §4, a prerequisite for the experiment rather than a consequence of it. The author thanks the staff of his nearest anatomical donation registry for confirming, in writing, that donated remains are not currently available for use as gravitational primaries in low-perturbation environments. He thanks separately the customer service department of a leading ballistic-gel manufacturer for clarifying that vacuum-rated 70-kg humanoid forms in SEBS formulation fall outside the company’s standard product line. Correspondence with the European Space Agency, the National Aeronautics and Space Administration, and the Japan Aerospace Exploration Agency regarding mission-of-opportunity slots on a future drag-free spacecraft for a chocolate confection and an anthropomorphic gravitational analogue is being drafted.

References

- Armano, M., Audley, H., Auger, G., et al. 2016, *Sub-Femto-g Free Fall for Space-Based Gravitational Wave Observatories: LISA Pathfinder Results*, Physical Review Letters, 116, 231101.
- Burns, J. A., Lamy, P. L., & Soter, S. 1979, *Radiation Forces on Small Particles in the Solar System*, Icarus, 40, 1.
- Fuchs, T. M., Uitenbroek, D. G., Plugge, J., et al. 2024, *Measuring Gravity with Milligram Levitated Masses*, Science Advances, 10, eadk2949.
- Garrett, H. B., & Whittlesey, A. C. 2012, *Guide to Mitigating Spacecraft Charging Effects*, JPL Space Science and Technology Series (Hoboken, NJ: Wiley).
- Gurnett, D. A., Kurth, W. S., Burlaga, L. F., & Ness, N. F. 2013, *In Situ Observations of Interstellar Plasma with Voyager 1*, Science, 341, 1489.
- Hamilton, D. P., & Burns, J. A. 1991, *Orbital Stability Zones About Asteroids*, Icarus, 92, 118.
- Heisler, J., & Tremaine, S. 1986, *The Influence of the Galactic Tidal Field on the Oort Comet Cloud*, Icarus, 65, 13.
- Hill, G. W. 1878, *Researches in the Lunar Theory*, American Journal of Mathematics, 1, 5.
- Landau, L. D., & Lifshitz, E. M. 1976, *Mechanics*, 3rd ed., Course of Theoretical Physics Vol. 1 (Oxford: Pergamon).
- Lauretta, D. S., Hergenrother, C. W., Chesley, S. R., et al. 2019, *Episodes of Particle Ejection from the Surface of the Active Asteroid (101955) Bennu*, Science, 366, eaay3544.
- Munroe, R. 2014, *Little Planet*, What If? #68, <https://what-if.xkcd.com/68/>.
- Rauf, M. A., & Ashraf, S. S. 2009, *Fundamental Principles and Application of Heterogeneous Photocatalytic Degradation of Dyes in Solution*, Chemical Engineering Journal, 151, 10.
- Richardson, J. D., Belcher, J. W., Garcia-Galindo, P., & Burlaga, L. F. 2019, *Voyager 2 Plasma Observations of the Heliopause and Interstellar Medium*, Nature Astronomy, 3, 1019.
- Scheeres, D. J. 1994, *Dynamics About Uniformly Rotating Triaxial Ellipsoids: Applications to Asteroids*, Icarus, 110, 225.

- Scheeres, D. J., Ostro, S. J., Hudson, R. S., & Werner, R. A. 1996, *Orbits Close to Asteroid 4769 Castalia*, Icarus, 121, 67.
- Scheeres, D. J., McMahon, J. W., French, A. S., et al. 2019, *The Dynamic Geophysical Environment of (101955) Bennu Based on OSIRIS-REx Measurements*, Nature Astronomy, 3, 352.
- Turyshev, S. G., Toth, V. T., Kinsella, G., Lee, S.-C., Lok, S. M., & Ellis, J. 2012, *Support for the Thermal Origin of the Pioneer Anomaly*, Physical Review Letters, 108, 241101.
- Westphal, T., Hepach, H., Pfaff, J., & Aspelmeier, M. 2021, *Measurement of Gravitational Coupling Between Millimetre-Sized Masses*, Nature, 591, 225.
- Whipple, E. C. 1981, *Potentials of Surfaces in Space*, Reports on Progress in Physics, 44, 1197.